Novel Data Acquisition Method for Interference Suppression in Dual-Channel SAR

Xiao-Hong Lin*, Guo-Yi Xue, and Pei-Guo Liu

Abstract—Various interference sources either intentional or unintentional can mask the synthetic aperture radar (SAR) signals and cause image degradation. With a novel data acquisition mode, a new method based on dual-channel SAR is applied to suppress the interference. Using the received dual-channel data, the two-dimensional location of the interference source can be estimated and then the interference can be removed via a Two-Channel-Cancelation method. By establishing a linear model of the interference-removed signal, the SAR image is reconstructed based on compressed sensing (CS) theory. Our method requires only a minor change to the traditional SAR system hardware while obtains a higher resolution. Simulation results are shown to demonstrate the validity of the proposed method.

1. INTRODUCTION

Synthetic aperture radar (SAR) can obtain high resolution images of illuminated scene under all weather circumstances, and it has been widely used in both civil remote sensing and military surveillance [1]. However, there exist various kinds of interferences, such as radio-frequency interference (RFI) and artificial interference [2, 3]. The RFI mainly comes from communication and television networks, while the artificial interference is generated by a military jammer. Also, these interferences are classified into two categories: 1) noncoherent interference; 2) coherent interference [4]. The noncoherent interference raises the noise level of SAR image to bury the targets of interest. In coherent interference, military jammer simulates target echoes or retransmits intercepted signals to cover the true target, then generates false targets in the scene, which affect the enemy commander's ability to judge the situation of the battlefield. Since the existence of these interferences would seriously degrade the quality of SAR imagery, SAR should embed the ability to detect and suppress the interferences.

At present, the suppression frameworks generally utilize the different characteristics between SAR and the interference in the following four aspects:

1) Signal form. [5] fits a multi-parameter model of the interference to the measured data and then coherently subtracting it. For nonstationary interference signals, this method is difficult to implement due to complicated model and high-dimensional parameter estimation. Based on a alteration of SAR transmitted signal, pulse diversity technologies are now widely applied to counter digital radio frequency memory (DRFM) repeat jammer [6–8], however they are incapable of suppressing the high-power noncoherent interference effectively.

2) Time-frequency domain. [4] utilizes wavelet to represent the instantaneous frequency of SAR received signal and designs a filter to filter the corresponding wavelet coefficients of the interference components. However, it requires the interference has good concentration in the time-frequency plane. In [9], the narrow band interference is obtained and canceled by subtracting different range subband spectra of the SAR image, but it is not suitable for removing wideband interference.

---

3) Space domain. Interferences can be removed using adaptive beamforming and space-time adaptive processing techniques [10–13]. These techniques work by forming the null adaptively in the interference direction to minimize interference. Nevertheless, many spatial degrees of freedom (DOF) may be required to attain full rejection whilst maintaining low sidelobes.

4) Polarization domain. In [14], the differences between SAR echo and coherent interference in polarization domain are analyzed and a method for discrimination and suppression of coherent interference in Doppler domain is proposed. However, it have limited performance in noncoherent interference suppression.

With the above analysis, a simplified SAR system with capacity in eliminating various types of interference would be potentially valuable in applications. To achieve this, a new interference suppression technique for dual-channel SAR is developed in this paper. First, we introduce a novel data acquisition method that requires only a minor change to the traditional SAR system hardware to work. At some randomly selected slow times, the new system receives SAR echoes contaminated with interference, while collecting only interference at the other slow times. The collected interferences are utilized to estimate the direction of arrival (DOA) angle of the interference source at the randomly selected slow times. Then, based on phase compensation in range frequency domain, the interference received at the randomly selected slow times can be removed via a Two-Channel-Cancelation (TCC) method. It will be demonstrated that the Signal-to-Interference ratio (SIR) is improved greatly by TCC operation. Finally, a linear model of the interference-removed signal is established and the SAR image is reconstructed based on the compressed sensing (CS) theory.

The remainder of this paper is organized as follows: Section 2 gives a basic introduction of CS principle. In Section 3, we introduce our data acquisition method and derive the imaging models in the presence of interference. Section 4 proposes a least square method to obtain the two-dimensional location of interference source and then the interference can be removed using dual-channel data. In Section 5, we use the interference-removed data to construct SAR image based on CS theory. The simulation results are listed in Section 6, and the paper is summarized in Section 7.

2. BASIS THEORY OF COMPRESSED SENSING

Before going into further explanations about our method, it is necessary to provide some background knowledge of compressed sensing (CS).

CS is a new theory which is available to reconstruct the sparse or compressible signals from far fewer measurements than required by Shannon-Nyquist sampling theorem. Assume that a discrete signal vector $\mathbf{x}_{N \times 1}$ is sparse on a basis matrix $\mathbf{\Psi}_{N \times N}$. $\mathbf{x}$ is represented as

$$\mathbf{x} = \mathbf{\Psi}\alpha \tag{1}$$

where $\alpha \in \mathbf{R}^N$ is the weighting coefficient with K nonzero elements and K a measure of the sparsity of $\mathbf{x}$.

According to CS theory, $\mathbf{x}$ is measured by a linear projections $\mathbf{y} = \mathbf{\Phi}\mathbf{x}$ where $\mathbf{\Phi} \in \mathbf{C}^{M \times N}$ with $M \ll N$. It makes sense that only M samples of $\mathbf{x}$ need to be measured instead of N. In a matrix notation, $\mathbf{y}$ is presented as

$$\mathbf{y} = \mathbf{\Phi}\mathbf{x} = \mathbf{\Phi}\mathbf{\Psi}\alpha = \mathbf{\Theta}\alpha \tag{2}$$

where $\mathbf{\Theta} = \mathbf{\Phi}\mathbf{\Psi} \in \mathbf{C}^{M \times N}$. Since $M < N$, this equation is an ill-posed problem and has infinitely many solutions. However, in CS theory, the sparse signal can be exactly reconstructed when the matrix $\mathbf{\Theta}$ has the Restricted Isometry Property (RIP) which requires:

$$(1 - \delta_k) \parallel \alpha \parallel_2 \leq \parallel \mathbf{\Theta}\alpha \parallel_2 \leq (1 + \delta_k) \parallel \alpha \parallel_2 \tag{3}$$

where $\delta_k \in (0, 1)$ is a minimal constant and α the sparse coefficient vector. It is proved that RIP can be achieved with high probability when $\mathbf{\Phi}$ is a random matrix [15].

Known the observed measurement $\mathbf{y}$ and the measured matrix $\mathbf{\Theta}$, the sparse vector α can be reconstructed by searching for the solution with a l_1 minimization criterion expressed as

$$\min \parallel \alpha \parallel_1 \quad \text{s.t } \mathbf{y} = \mathbf{\Theta}\alpha \tag{4}$$

if noise is taken into account, the above problem is changed into:

$$\min \lambda \parallel \alpha \parallel_1 \quad \text{s.t} \quad \parallel \mathbf{y} - \boldsymbol{\Theta}\alpha \parallel_2 < \varepsilon \tag{5}$$

where λ is a weighted coefficient, and ε bounds the amount of noise in measured data.

Computation of (4) and (5) are both convex problems. Recently, there is a variety of sparse approximation algorithms for solving such problems such as basis pursuit (BP) [16] and orthogonal matching pursuit (OMP) [17].

3. DUAL-CHANNEL SAR IMAGING MODEL

3.1. Signal Model and Interference Model

In this paper, we consider a SAR system working in stripmap mode and having 2 antennas placed along the azimuth direction with the inner spacing d. The first antenna transmits radar pulses and both antennas receive the scattered echo signals. The observation mode of dual-channel SAR is shown in Fig. 1. $C1$ and $C2$ denote the first and the second antenna respectively. Axis X, Y and Z are corresponding to the azimuth, range and height direction respectively. By setting the scene center to be the origin, the transmitter is located at (vt_a, y_s, H), and the other receive antenna is at $(vt_a + d, y_s, H)$ where t_a is the slow time and v is the velocity of the platform.
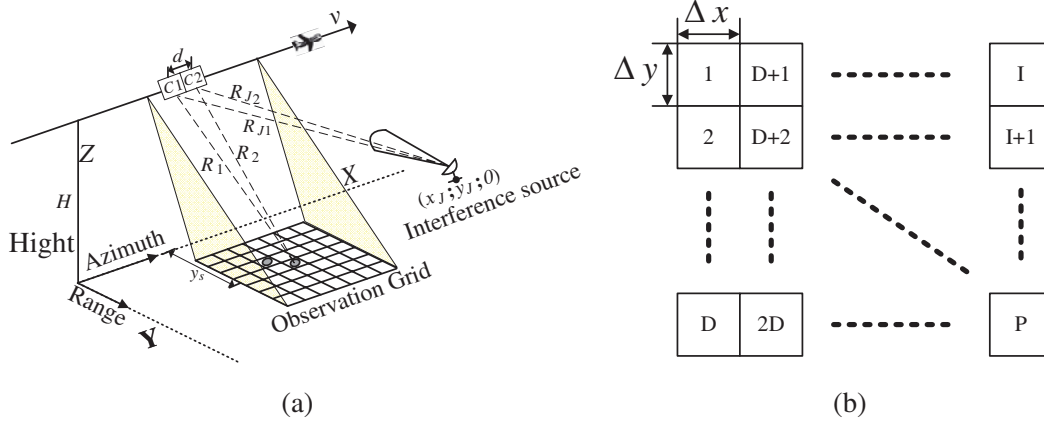

Figure 1. Observation geometry of dual-channel SAR. (a) The stripmap geometry; (b) Observation grids.

The beam footprint is divided into P equal observation cells, as shown in Fig. 1(b). The sparse targets will be located on the corresponding grid nodes. The size of every observation cell is $\Delta x \times \Delta y$ where $\Delta x = vT_a$, $\Delta y = c \times T_s/2$, T_a is the pulse repetition interval (PRI) of SAR, c is the velocity of light and T_s is the range sampling period. Here, every cell is assigned a index i ($i = 1, 2, 3, \ldots, P$). The targets location information obviously depends on the observation grid.

Suppose the radar transmit signal is

$$s_t(t_r) = p(t_r)\exp(j2\pi f_c t_r) \tag{6}$$

where t_r is the fast time, f_c the carrier frequency, and $p(t_r)$ i the transmitted waveform which can be written as

$$p(t_r) = \text{rect}\left(\frac{t_r}{T_p}\right)\exp(j\pi\gamma t_r^2) \tag{7}$$

Here, rect($\cdot$) is the rectangle window, T_p the pulse duration, and γ the chirp rate.

Considering the movement of the radar platform along azimuth direction, the ground echo received by the kth ($k = 1, 2$) channel can be written as

$$s_k(t_a, t_r) = \sum_{i=1}^{P} g(i)p\left(t_r - \frac{R_{sk}(t_a, i)}{c}\right)\exp\left(-\frac{j2\pi f_c R_{sk}(t_a, i)}{c}\right) \tag{8}$$

where $g(i)$ is the average backscattering coefficient of the corresponding discrete cell, and $R_{sk}(t_a, i)$ is represented as follow

$$R_{s1}(t_a, i) = 2R_1(t_a, i)$$
$$R_{s2}(t_a, i) = R_1(t_a, i) + R_2(t_a, i)$$

(9)

where $R_1(t_a, i) = \sqrt{(vt_a - x_i)^2 + y_i^2 + H^2}$ is the range from $C1$ to the target located at $(x_i, y_i, 0)$ and $R_2(t_a, i) = \sqrt{(vt_a + d - x_i)^2 + y_i^2 + H^2}$ the distance between $C2$ and this target.

Assume there exists a interference sources at $(x_J, y_J, 0)$, as shown in Fig. 1(a). The ranges from $C1$ and $C2$ to the interference source are $R_{J1}(t_a)$ and $R_{J2}(t_a)$, respectively. In a far-field condition, $R_{J2}(t_a) - R_{J1}(t_a) \approx d\sin(\theta_J(t_a))$ where $\theta_J(t_a)$ is the direction of arrival (DOA) angle of the interference signal [18]. Then, the interference signal received by $C2$ can be expressed as

$$z_2(t_a, t_r) = z_1\left(t_a, t_r - \frac{d\sin(\theta_J(t_a))}{c}\right)$$

(10)

where $z_1(t_a, t_r)$ is the received interference signal in the first channel.

3.2. Data Acquisition

Traditional SAR system consists of transmitter, T/R switch, antenna and data recorder. The T/R switch directs the pulse to the first antenna and returned echo to both the two receivers at an uniform pulse repetition interval (PRI). Our new data acquisition system is almost similar to the traditional one, the only difference being that there exists a diode switch in the transmit module,as shown in Fig. 2(a). This diode switch is controlled by a random 0/1 sequence. When the number is 1, a high positive voltage is applied on the diode anode and the diode is forward biased. In effect, this diode switch is closed and the SAR works the same as the traditional system. When the number becomes 0, a positive voltage is applied on the cathode and the diode is reverse biased. In this situation, the diode switch is opened and both the two antennas only receive electromagnetic wave without transmitting a pulse. The random 0/1 sequence can be generated before SAR data acquisition. When SAR works, the random number is refreshed at every PRI. Fig. 2(b) shows the difference between traditional SAR and our novel data acquisition. In Fig. 2(b), the traditional SAR transmits the pulse (denoted by the rectangle window) toward the area to be imaged and collects return electromagnetic wave (represented by the red curve) at every PRI. If there exists interference, these received signals contain the ground echoes and the interference. For our acquisition system, when the random number is 1, the radar receive the echoes and interference which are the same as the traditional SAR. However, the new system only receives interference (denoted by the green curve) when the random number is 0.
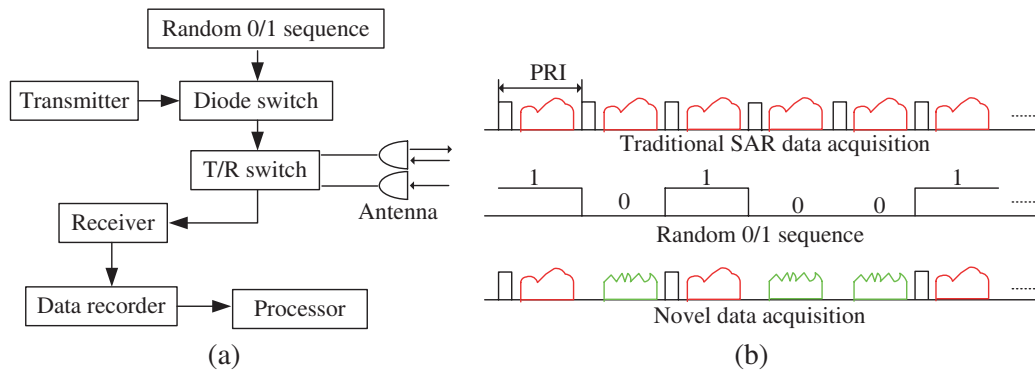

Figure 2. Data acquisition method proposed in this paper. (a) Basic block diagram of the system; (b) Comparison with traditional SAR. (Red curve: SAR echoes contaminated with interference; Green curve: interference).

In this paper, the azimuth time when SAR transmits a pulse is denoted as t_{at}, and the azimuth time when SAR only receive interference signal is represented as t_{ar}. Ignoring the propagation effect of the electromagnetic, the complete signals received by the kth receiver can be expressed as follow

$$e_k(t_a, t_r) = \begin{cases} s_k(t_a, t_r) + z_k(t_a, t_r) & \text{if} \quad t_a = t_{at} \\ z_k(t_a, t_r) & \text{if} \quad t_a = t_{ar} \end{cases} \tag{11}$$

4. INTERFERENCE SUPPRESSION USING DUAL-CHANNEL DATAS

4.1. Removing Interference

From (10) and (11), at the slow time t_{at}, the output of SAR in the range frequency domain is represented by

$$E_1(t_{at}, f_r) = S_1(t_{at}, f_r) + Z_1(t_{at}, f_r) \tag{12}$$

$$E_2(t_{at}, f_r) = S_2(t_{at}, f_r) + \exp\left(-j2\pi f_r \frac{d\sin(\theta_J(t_{at}))}{c}\right) Z_1(t_{at}, f_r) \tag{13}$$

where E_k, S_k and Z_k denote the range spectrum of the total received signal, real echoes and interference signal in the kth channel, respectively. According to the above two formulas, the interference can be removed by a Two-Channel-Cancelation (TCC) method based on phase compensation, if $\theta_J(t_{at})$ is known. After TCC processing, the residual echoes will become

$$E_2(t_{at}, f_r) - \beta(t_{at}, f_r)E_1(t_{at}, f_r) = S_2(t_{at}, f_r) - \beta(t_{at}, f_r)S_1(t_{at}, f_r) \tag{14}$$

where $\beta(t_{at}, f_r) = \exp\left(-j2\pi f_r d\sin(\theta_J(t_{at}))/c\right)$. Based on this formula, the illuminated scene can be reconstructed via CS, which will be discussed in Section 5. However, $\theta_J(t_a)$ is unknown. In Subsection 4.2, we will derive these DOAs in high precision, utilizing the data received at the slow time t_{ar}.

4.2. Two Dimensional Location of Interference Source

According to the geometrical relationship between SAR and the interference source, as shown in Fig. 3, a formula can be obtained as

$$\tan(\theta_J(t_{ar})) = \frac{vt_{ar} - x_J}{\sqrt{y_J^2 + H^2}} = Qt_{ar} + b \tag{15}$$

where $Q = v/\sqrt{y_J^2 + H^2}$, $b = -x_J/\sqrt{y_J^2 + H^2}$ and $\theta_J(t_{ar})$ can be estimated by these methods [19–21]. It should be noted that $\tan(\theta_J(t_{ar}))$ form a straight line with slope Q and intercept b for real DOA values $\theta_J(t_{ar})$. However, for the estimated DOA values $\hat{\theta}_J(t_{ar})$, $\tan(\hat{\theta}_J(t_{ar}))$ will fluctuate around this straight line. In order to obtain the DOAs of the interference source at the slow time t_{at}, an operation
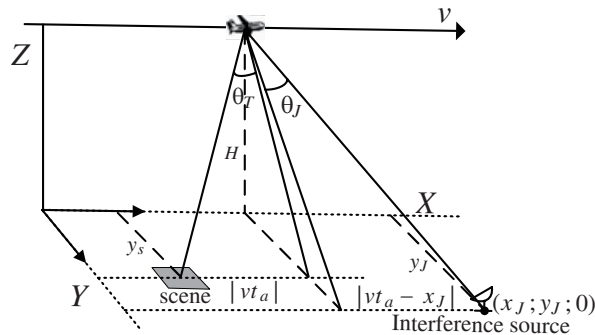

Figure 3. The geometry between SAR and the interference source.

called linear least-squares fitting is carried out to a set of $(t_{ar}, \tan(\hat{\theta}_J(t_{ar})))$ data pairs. Then, we will obtain a fitting straight line whose slope $\hat{Q}$ and intercept $\hat{b}$ can be expressed as [22]

$$\hat{Q} = \frac{\overline{t_{ar}t_{an}} - \overline{t_{ar}} \cdot \overline{t_{an}}}{\overline{t_{ar}^2} - \overline{t_{ar}}^2} \tag{16}$$

$$\hat{b} = \frac{\overline{t_{ar}^2} \cdot \overline{t_{an}} - \overline{t_{ar}} \cdot \overline{t_{ar}t_{an}}}{\overline{t_{ar}^2} - \overline{t_{ar}}^2} \tag{17}$$

respectively, where symbols with an overline denote average values and $t_{an} = \tan(\hat{\theta}_J(t_{ar}))$. Since the least-squares solutions are unbiased, consistent and effective, it means that the estimated parameters have the highest probability to be correct and will converge toward the true values when the azimuth sample number of the interference increases. From $\hat{Q}$ and $\hat{b}$, the two-dimensional location of the jammer can be realized, and the corresponding coordinate can be derived as

$$\hat{x}_J = -\frac{v\hat{b}}{\hat{Q}} \tag{18}$$

$$\hat{y}_J = \sqrt{\frac{v^2}{\hat{Q}^2} - H^2} \tag{19}$$

Then, $\sin(\theta_J(t_{at}))$ can be estimated by

$$\sin\left(\hat{\theta}_J(t_{at})\right) = \frac{vt_{at} - \hat{x}_J}{\sqrt{(\hat{x}_J - vt_{at})^2 + \hat{y}_J^2 + H^2}} \tag{20}$$

Now, we can remove the interference signal using the method proposed in Subsection 4.1.

4.3. Suppression Performance Analysis

Actually, due to the estimation error of $\sin(\theta_J(t_{at}))$, the interference will not be removed completely. Next, we will analyze the change of the Signal-to-Interference ratio (SIR) after TCC processing. For simplicity, in this subsection, we ignore the indexes related to f_r and t_{at}.

After TCC, the residual signal can be expressed as follow

$$\Delta E = E_2 - \beta(\hat{\theta}_J)E_1 = S_2 - \beta(\hat{\theta}_J)S_1 + \left(\beta(\theta_J) - \beta(\hat{\theta}_J)\right)Z_1 \tag{21}$$

Approximately, we can regard the real echoes as the signal transmitted by a source located in the center of the illuminated scene. Then, the echoes have the same property with the interference described by (10). Now, ΔE can be rewritten as

$$\Delta E = \left(\beta(\theta_T) - \beta(\hat{\theta}_J)\right)S_1 + \left(\beta(\theta_J) - \beta(\hat{\theta}_J)\right)Z_1 \tag{22}$$

We define SIR before TCC as $SIR_{orig} = |S_1/Z_1|^2$. Then, after TCC, the SIR becomes

$$SIR_{TCC} = \vartheta \cdot SIR_{orig} = \left|\frac{\beta(\theta_T) - \beta(\hat{\theta}_J)}{\beta(\theta_J) - \beta(\hat{\theta}_J)}\right|^2 SIR_{orig} \tag{23}$$

where ϑ is the SIR improvement factor.

In general, the SAR bandwidth $B \ll fc$. For DOA determination with no ambiguity, it requires that the antenna spacing $d \le \lambda/2$ where λ is the carrier wavelength of SAR [18]. Here, we set d to be a typical value $\lambda/2$. Then, $\beta(\theta) \approx \exp(-j2\pi d\sin(\theta)/\lambda) = \exp(-j\pi\sin(\theta))$ and ϑ can be rewritten as

$$\vartheta = \left|\frac{\exp\left(-j\pi\frac{\sin(\theta_T)-\sin(\hat{\theta}_J)}{2}\right) - \exp\left(j\pi\frac{\sin(\theta_T)-\sin(\hat{\theta}_J)}{2}\right)}{\exp\left(-j\pi\frac{\sin(\theta_J)-\sin(\hat{\theta}_J)}{2}\right) - \exp\left(j\pi\frac{\sin(\theta_J)-\sin(\hat{\theta}_J)}{2}\right)}\right|^2 \times \left|\frac{\exp\left(-j\pi\frac{\sin(\theta_T)+\sin(\hat{\theta}_J)}{2}\right)}{\exp\left(-j\pi\frac{\sin(\theta_J)+\sin(\hat{\theta}_J)}{2}\right)}\right|^2$$

$$= \left|\frac{\sin\left(\frac{\pi}{2}\left(\sin(\theta_T) - \sin(\hat{\theta}_J)\right)\right)}{\sin\left(\frac{\pi}{2}\left(\sin(\theta_J) - \sin(\hat{\theta}_J)\right)\right)}\right|^2 = \left|\frac{\sin\left(\frac{\pi}{2}\left(\sin(\theta_T) - \sin(\hat{\theta}_J)\right)\right)}{\sin\left(\pi\cos\left(\frac{\theta_J+\hat{\theta}_J}{2}\right)\sin\left(\frac{\theta_J-\hat{\theta}_J}{2}\right)\right)}\right|^2 \tag{24}$$

For side-looking SAR, $\sin(\theta_T) \approx 0$. When the estimation error $\Delta\theta_J = |\theta_J - \hat{\theta}_J| \ll 1$, we have

$$\vartheta \approx \left| \frac{\sin\left(\frac{\pi}{2}\sin\left(\hat{\theta}_J\right)\right)}{\sin\left(\frac{\pi}{2}\cos(\theta_J)\left(\theta_J - \hat{\theta}_J\right)\right)} \right|^2 \approx \left| \frac{\sin\left(\frac{\pi}{2}\sin(\theta_J)\right)}{\frac{\pi}{2}\cos(\theta_J)\Delta\theta_J} \right|^2 \qquad (25)$$

Figure 4 shows the SIR improvement factors under different DOA estimation errors. It can be seen that ϑ improves greatly when the DOA estimation accuracy becomes higher. In addition, when θ_J gets larger, the improvement factor also grows higher.

In theory, we can obtain a satisfied DOA estimation accuracy using the method proposed in Subsection 4.2, when SAR receives enough interference signals. That is to say, after TCC processing, the interference can be removed effectively.
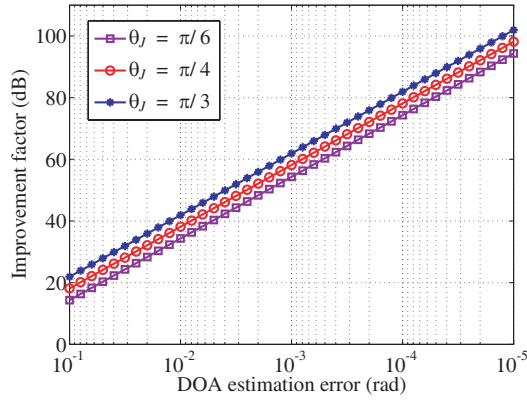

Figure 4. The SIR improvement factor versus the DOA estimation error.

5. SAR IMAGE RECONSTRUCTION BASED ON CS

After TCC processing, the SAR image is unable to be obtained via the traditional imaging algorithms. However, we can reconstruct the sparse scene based on CS theory.

In order to use CS, a linear measurement model of the interference-removed signals should be created firstly.

5.1. The Linear Model for Interference-Removed Signal

In practice, the range and azimuth times are discrete due to the sampling process. The 2-D discrete time SAR echoes $s_k(t_{at}, t_r)$ can be written as $s_k(t_{a,m}, t_{r,n})$, $m = 1, 2, \ldots, M$, $n = 1, 2, \ldots, N$ where M is the number of azimuth samples and N is the number of samples for each pulse.

(8) can be expressed in matrix form as

$$\mathbf{s}_k = \mathbf{A}_k \mathbf{g} \qquad (26)$$

where $\mathbf{s}_k$ is an $MN \times 1$ vector, $\mathbf{A}_k$ an $MN \times P$ matrix, and $\mathbf{g}$ the $P \times 1$ scattering coefficient vector. Here, $\mathbf{g}$ is sparse and only $K(K \ll P)$ of its components is nonzero or greater than zero. In the above expression,

$$\mathbf{s}_k = [s_k(t_{a,1}, t_{r,1}), \ldots, s_k(t_{a,1}, t_{r,N}), s_k(t_{a,2}, t_{r,1}), \ldots, s_k(t_{a,2}, t_{r,N}), \ldots, s_k(t_{a,M}, t_{r,1}), \ldots, s_k(t_{a,M}, t_{r,N})]^{\mathrm{T}} \qquad (27)$$

Let

$$\phi(t_{a,m}, t_{r,n}, i) = p(t_{r,n} - R_{sk}(t_{a,m}, i)/c) \exp\left(-j2\pi f_c R_{sk}(t_{a,m}, i)/c\right) \qquad (28)$$

Then, the projection matrix can be expressed as

$$\mathbf{A}_k = [\mathbf{a}(t_{a,1}, t_{r,1}), \ldots, \mathbf{a}(t_{a,1}, t_{r,N}), \mathbf{a}(t_{a,2}, t_{r,1}), \ldots, \mathbf{a}(t_{a,2}, t_{r,N}), \ldots, \mathbf{a}(t_{a,M}, t_{r,1}), \ldots, \mathbf{a}(t_{a,M}, t_{r,N})]^{\mathrm{T}} \qquad (29)$$

where
$$\mathbf{a}(t_{a,m}, t_{r,n}) = [\phi(t_{a,m}, t_{r,n}, 1), \phi(t_{a,m}, t_{r,n}, 2), \ldots, \phi(t_{a,m}, t_{r,n}, P)] \tag{30}$$

Also, $S_k(t_{at}, f_r)$ can be rewritten as

$$\mathbf{S}_k = \mathbf{\Omega}\mathbf{s}_k = \mathbf{\Omega}\mathbf{A}_k\mathbf{g} \tag{31}$$

where $\mathbf{\Omega}$ is a $MN \times MN$ matrix represented as follow

$$\mathbf{\Omega} = \begin{bmatrix} \mathbf{F} & \mathbf{0} & \cdots & \mathbf{0} \\ \mathbf{0} & \mathbf{F} & \cdots & \mathbf{0} \\ \mathbf{0} & \mathbf{0} & \ddots & \mathbf{0} \\ \mathbf{0} & \mathbf{0} & \cdots & \mathbf{F} \end{bmatrix} \tag{32}$$

Here, $\mathbf{F}$ is a $N \times N$ discrete Fourier transformation (DFT) matrix with the (p, q)th entity given by $1/\sqrt{N}\exp(-j2\pi pq/N)$.

Similarly, (14) can be expressed in a matrix form as

$$\mathbf{E}_2 - \mathbf{B}\mathbf{E}_1 = \mathbf{S}_2 - \mathbf{B}\mathbf{S}_1 = (\mathbf{\Omega}\mathbf{A}_2 - \mathbf{B}\mathbf{\Omega}\mathbf{A}_1)\mathbf{g} \tag{33}$$

where $\mathbf{E}_k$ is a $MN \times 1$ vector and has a similar construction to $\mathbf{S}_k$; $\mathbf{B}$ is a $MN \times MN$ matrix defined as

$$\mathbf{B} = \begin{bmatrix} \mathbf{B}_1 & \mathbf{0} & \mathbf{0} & \cdots & \mathbf{0} \\ \mathbf{0} & \mathbf{B}_2 & \mathbf{0} & \cdots & \mathbf{0} \\ \vdots & \vdots & \ddots & \vdots & \vdots \\ \mathbf{0} & \mathbf{0} & \mathbf{0} & \mathbf{B}_{M-1} & \mathbf{0} \\ \mathbf{0} & \mathbf{0} & \mathbf{0} & \mathbf{0} & \mathbf{B}_M \end{bmatrix} \tag{34}$$

where $\mathbf{B}_m$ is a $N \times N$ matrix defined as

$$\mathbf{B}_m = \begin{bmatrix} \beta(t_{a,m}, f_{r,1}) & 0 & \cdots & 0 \\ 0 & \beta(t_{a,m}, f_{r,2}) & \cdots & 0 \\ \vdots & \vdots & \ddots & \vdots \\ 0 & 0 & \cdots & \beta(t_{a,m}, f_{r,N}) \end{bmatrix} \tag{35}$$

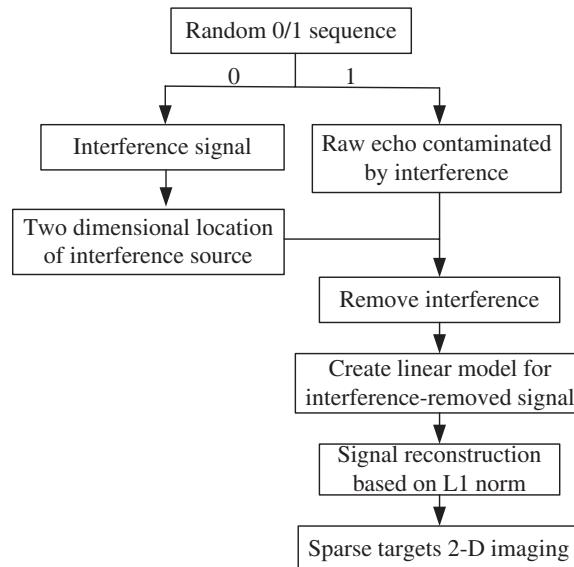Here, $\beta(t_{a,m}, f_{r,n})$ is the 2-D discrete form of $\beta(t_{at}, f_r)$.

Figure 5. The flow chart of the presented interference suppression method for SAR imaging.

5.2. Signal Reconstruction by CS

In our data acquisition method, the collection of SAR echo from the illuminated scene is equivalent to random slow time undersampling. In the spirit of CS, a very small number of "random" measurements carry enough information which can accomplish completely reconstruction for the signal. Let $\mathbf{E}' = \mathbf{E}_2 - \mathbf{B}\mathbf{E}_1$ be the undersampled data expressed in frequency domain, and $\mathbf{A}' = \mathbf{\Omega}\mathbf{A}_2 - \mathbf{B}\mathbf{\Omega}\mathbf{A}_1$ be the projection matrix. Then, our CS measurement can be written as

$$\mathbf{E}' = \mathbf{A}'\mathbf{g} \tag{36}$$

If the SAR image is sparse or compressible, then the targets can be reconstructed by solving [23]

$$\min \|\mathbf{g}\|_1 \qquad \text{s.t. } \mathbf{A}'\mathbf{g} = \mathbf{E}' \tag{37}$$

The main flow chart of imaging algorithm for SAR based on CS is shown in Fig. 5.

Currently, many SAR imaging methods based on CS have been introduced [23–26]. It is demonstrated that these methods improve the radar ability and image quality benefited from the application of CS theory. Also, our method offers the similar advantages.

(1) Reduction in Data

In many SAR systems, radar data is directly stored on board and then transmitted to the ground. In [25], the authors proposed to transmit fewer pulses than traditional systems at random intervals, instead of transmitting pulses with a regular PRI. This scheme is known as "random slow-time undersampling" which is similar to our acquisition for the contaminated SAR echo. In addition, the interference is not necessary to be stored. We can estimate the DOA on board and transmit the results to ground. Thus, Our system has the potential to significantly reduce the amount of data to be stored and transmitted.

(2) Higher Resolution

The resolution of conventional SAR imaging algorithm based on Matched Filter (MF) theory is limited by the transmitted signal bandwidth and the antenna length. In [24], a conclusion is drawn that the sidelobe is suppressed significantly and a higher resolution can be obtained via a sparse reconstruction method. Similarly, our method also can image the sparse scene with a higher resolution than the traditional SAR.

(3) Obtaining Wider Swaths

For the traditional SAR, azimuth undersampling at the rate of the pulse repetition frequency causes azimuth ambiguity, which induces ghost into the images. [26] has proved that azimuth random sampling can suppress azimuth ambiguity effectively. Thus, our method is possible to image a much wider swath than possible by the conventional methods.

6. SIMULATION AND ANALYSIS

In order to evaluate the performance of the presented method, some numerical simulation results are provided in this section. The system parameters are shown as follows: carrier wavelength $\lambda = 6$ cm, the bandwidth of LFM signal $B_r = 60$ MHz, pulse duration $T_r = 1$ μs, sample rate $f_s = 84$ MHz, pulse repetition frequency $f_p = 300$ Hz, SAR velocity $v = 400$ m/s, slant range of scene center is 10 km and antenna interval $d = 3$ cm($\lambda/2$). Assume there exists a interference source located at (1000 m, 500 m, 0 m), transmitting wideband noise signals. The signal-to-interference ratio (SIR) is set to be -30 dB. In this section, the simulations of two scenes are tested, one is a sample scene has nine point targets, and another is a complex scene has a ship from ERS SAR image. The original scenes and their imaging results of the traditional SAR with interference are shown in Fig. 6. Due to the interference, the targets smears and SAR is unable to perform accurate target detection and parameter estimation.
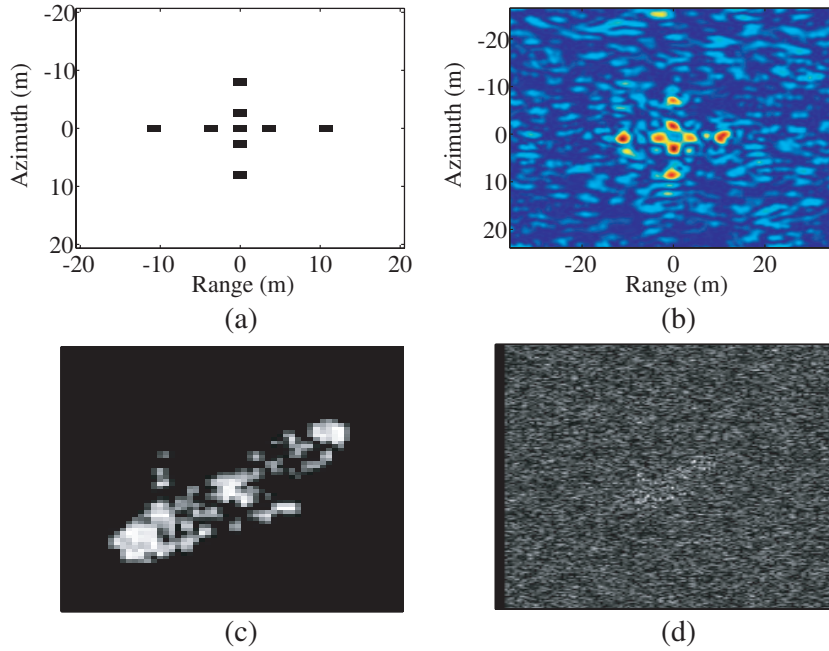
Figure 6. The simulated scene. (a) and (b) Nine point targets and its imaging result of the traditional SAR with interference; (c) and (d) A ship from ERS SAR image and its imaging result of the traditional SAR with interference.

6.1. Point Target Simulation

The signal-to-noise ratio (SNR) is 15 dB and the radar works in our data acquisition method, and the numbers of slow-time samples when the transmitter works is set to be 50 (35% of all azimuth samples). First, we use the interference signal received at t_{ar} to locate and remove the interference. The DOA values of the interference source is estimated with the two-side correlation transformation (TCT) algorithm [19]. As shown in Fig. 7(a), the tangent values of the estimated DOA fluctuate around the fitting straight line whose slope is 0.0378 and intercept is -0.0959. According to (18) and (19), the interference source can be located at (1015.1 m, 590.71 m, 0 m). Based on (20), the sine values of the interference DOA can be estimated in a high precision, as shown in Fig. 7(b). The average estimation accuracy of the interference's DOA is 0.0052 rad and the SIR improvement factor is 51.38 dB. In other word, SIR becomes 21.38 dB after TCC operation. Then, the corresponding linear model can be established. Using the sparse information of the target space and solving the convex optimization problem, the result of the presented method is shown in Fig. 8(a). It is observed that the interference is removed and the actual target are clearly reconstructed compared with the traditional SAR imaging algorithm shown in Fig. 8(b). In addition, the value of sidelobe in our method is far less than that in tradition SAR, and the resolution is improved greatly.

In our method, there are two parameters which have an important influence on the interference suppression performance. The first one is SNR and the other is the ratio σ defined as ε/ζ, where ε denotes the number of slow-time samples when SAR transmitter works and ζ represents that of all slow-time samples. We use relative error (RE) of the reconstruction image to evaluate the method performance. The RE is defined as follow.

$$RE = \sqrt{\frac{\sum\limits_{i=1}^{P} [\hat{g}(i) - g(i)]^2}{\sum\limits_{i=1}^{P} g(i)^2}} \tag{38}$$

where $g(i)$ denotes the original image sequence of scattering coecients for illuminated scene, and $\hat{g}(i)$
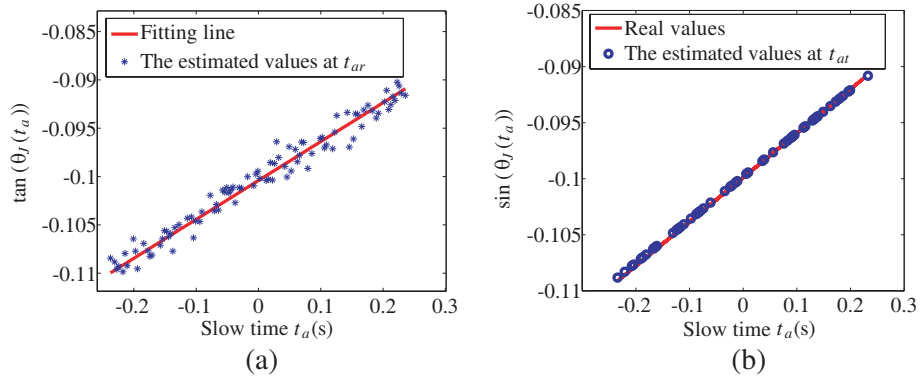
Figure 7. The estimated DOA values of the interference source. (a) Tangent values of the estimated DOA at slow time t_{ar}; (b) Sine values of the estimated DOA at slow time t_{at}.
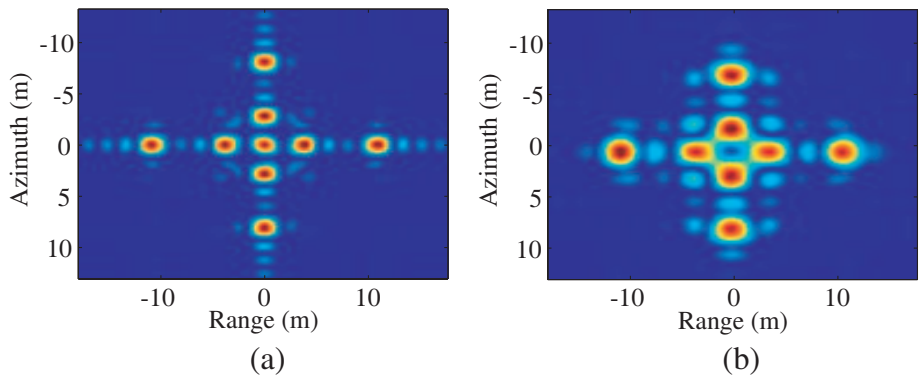

Figure 8. The imaging result of the nine point targets. (a) The proposed method; (b) The traditional SAR without interference.
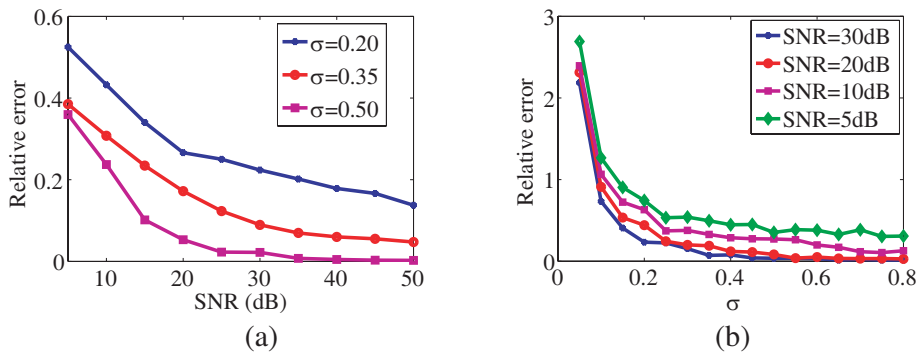

Figure 9. The relative error of target reconstruction by the proposed method. (a) The RE versus SNR under different σ; (b) The RE versus the ratio σ under different SNR.

is the reconstructed one. Apparently, the lower the value of RE is, the better the performance will be. Fig. 9 shows the RE of the constructed image versus the different ratio σ and different SNR. At each SNR level or ratio σ, 100 independent trial are performed. In Fig. 9(a), the result demonstrates that the method performance deteriorates with the decreases of SNR. It is because that the CS reconstruction is sensitive to noise [24]. In our simulations, the targets were still reconstructed correctly but with some false targets coming out when SNR is 5 dB. Fig. 9(b) plots the RE of the proposed method at different ratio σ under different SNR. It is observed that RE becomes smaller when the ratio σ increases, and a satisfied imaging result can be obtained when σ is more than 0.2.

6.2. Ship Scene Simulation

The ship echo signals are added by Gaussian white noise with different SNR levels (SNR = 5 dB, 10 dB, 20 dB) when the interference source locates at (1000 m, 0 m, 0 m) and $\sigma = 0.35$. After interference suppression, the imaging results of the ship are shown in Fig. 10(a). It can be seen that the locations and scattering coefficients of ship scene are well extracted with low sidelobe by our method at high SNR level. However, in low SNR level (such as 5 dB), the image is deteriorated. There are two reasons. One is that CS is sensitive to noise. The other one is that lower SNR will bring about lower DOA estimation accuracy and SIR improvement factor.

Under SNR = 20 dB and $\sigma = 0.35$, the interference source is located at different coordinates: (100 m, 0 m, 0 m), (500 m, 0 m, 0 m) and (2000 m, 0 m, 0 m). The corresponding DOA of the interference are approximately 0.57°, 2.86° and 11.46° during the imaging time. The final imaging results of the presented method is shown in Fig. 10(b). We can see that when the interference source is separated farther away from the imaging scene, a better imaging result will be obtained. It is because that larger DOA of the interference will result in a higher SIR improvement factor, which has been proved in Subsection 4.3.

Finally, we set SNR = 20 dB, the interference source to be at (1000 m, 0 m, 0 m) while $\sigma = 0.15$, 0.35 and 0.55 respectively. The imaging results are shown in Fig. 10(c). These results show that the quality of SAR image will be improved with larger σ. This is because the better performance of CS
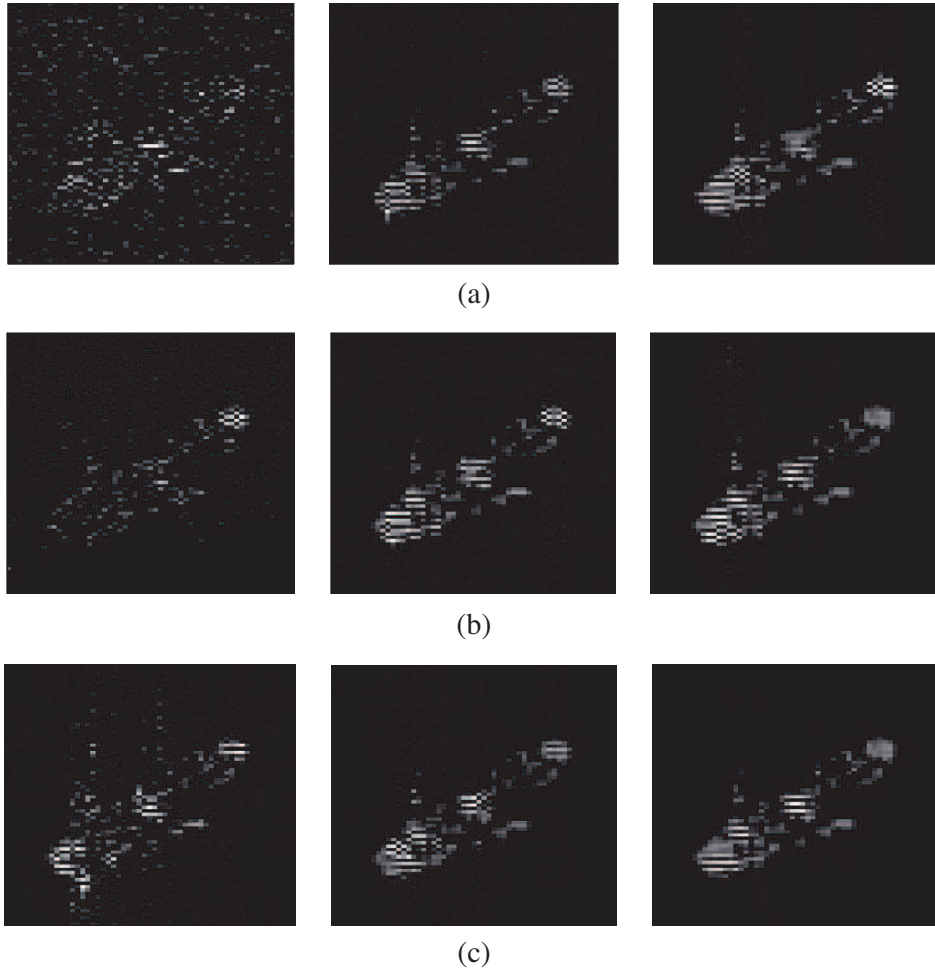

(a)

(b)

(c)

Figure 10. The imaging results of a ship scene under different condition. (a) Different SNR (left: 5 dB, middle: 10 dB, right: 20 dB); (b) Different DOA of the interference (left: $\theta_J \approx 0.57°$, middle: $\theta_J \approx 2.86°$, right: $\theta_J \approx 11.46°$); (c) Different σ (left: $\sigma = 0.15$, middle: $\sigma = 0.35$, right: $\sigma = 0.55$).

relies on the larger number of measurements [24]. In other words, the larger the number of echo samples are, the more scattering centers can be reconstructed.

7. CONCLUSION

Image degradation due to various interferences is an important problem in SAR imaging, which can not neglected during SAR image analysis. With a novel data acquisition mode, this paper has proposed a new interference suppression method for dual-channel SAR. Compared to conventional interference suppression approaches, the proposed method can obtain the two-dimensional location of the interference source, which is an important information for Electronic Counter Counter Measures. In addition, reduction in data, higher resolution and wider swaths can be achieved. However, there exist two constraints for this method. First, the illuminated scene should be sparse or compressible. Second, there is only one interference source located in the sidelobe region. In the future, we will extend this work to remove multiple interferences with multi-channel SAR.

ACKNOWLEDGMENT

REFERENCES

1. Chan, Y. K. and V. C. Koo, "An introduction to synthetic aperture radar (SAR)," *Progress In Electromagnetics Research B*, Vol. 2, 27–60, 2008.
2. Liu, Q., J. Dong, X. Wang, S. Xing, and B. Pang, "An efficient SAR jammer with direct radio frequency processing (Drfp)," *Progress In Electromagnetics Research*, Vol. 137, 293–309, 2013.
3. Wu, X., D. Dai, and X. Wang, "Study on SAR jamming measures," *IET International Conference on Radar Systems*, 176–179, Edinburgh, England, 2007.
4. Zhou, F., R. Wu, M. Xing, and Z. Bao, "Interference suppression algorithm for SAR based on time-frequency transform," *IEEE Transaction on Geoscience and Remote Sensing*, Vol. 49, 3765–3779, 2011.
5. Lord, R. T. and M. R. Inggs, "Efficient RFI suppression in SAR using LMS adaptive filter integrated with range/Doppler algorithm," *Electronic Letter*, Vol. 35, 629–630, 1999.
6. Soumekh, M., "SAR-ECCM using phase-perturbed LFM chirp signals and DRFM repeat jammer penalization," *IEEE Transactions on Aerospace and Electronic Systems*, Vol. 42, 191–205, 2006.
7. Lu, G., B. Tang, and G. Gui, "Deception ECM signals cancellation processor with joint time-frequency pulse diversity," *IEICE Electronics Express*, Vol. 8, 1608–1613, 2011.
8. Li, W., X. L. Wang, and X. M. Wang, "Anti-jamming techniques for synthetic aperture radar," *Proc. IEEE International Geoscience and Remote Sensing Symposium*, 605–608, 2009.
9. Feng, J., H. Zheng, Y. Deng, and D. Gao, "Application of subband spectral cancellation for SAR narrow-band interference suppression," *IEEE Geoscience and Remote Sensing Letters*, Vol. 9, 190–193, 2012.
10. Guerci, *Space-time Adaptive Processing for Radar*, Artech House, 2003.
11. Paine, A. S., "An adaptive beamforming technique for countering synthetic aperture radar (SAR) jamming threats," *IEEE 2007 Radar Conference*, 630–634, 2007.
12. Rosenberg, L. and D. Gray, "Anti-jamming techniques for multichannel SAR imaging," *IEE Proceedings: Radar, Sonar and Navigation*, Vol. 153, 234–242, 2006.
13. Rosenberg, L. and D. Gray, "Constrained fast-time STAP for interference Suppression in multichannel SAR," *IEEE Transaction on Aerospace and Electronic Systems*, Vol. 49, 1792–1805, 2013.
14. Dai, D. H., X. S. Wang, S. P. Xiao, and Y. Z. Li, "Discrimination and suppression of active-decoys jamming in PolSAR," *Acta Electronica Sinica*, Vol. 9, 1779–1783, 2007.

15. Baraniuk, R., "Compressive sensing," *IEEE Signal Processing*, Vol. 24, No. 4, 118–121, 2007.

16. Candes, E. J., J. Romberg, and T. Tao, "Robust uncertainty principles: Exact signal reconstruction from highly incomplete frequency information," *IEEE Transaction on Information Theory*, Vol. 52, 489–509, 2006.

17. Tropp, J. A., "Greed is good: Algrorithm results for sparse approximation," *IEEE Transaction on Information Theory*, Vol. 50, 2231–2242, 2004.

18. Chen, Z. Z., G. Gokeda, and Y. Q. Yu,, *Introduction to Direction-of-arrival Estimation* , Artech House, 2010.

19. Valaee, S. and P. Kabal, "Wideband array processing using a two-sided correlation transformation," *IEEE Transactions on Signal Processing*, Vol. 43, 160–172, 1995.

20. Reddy, V. V., B. Ng, Y. Zhang, and A. W. Khong, "DOA estimation of wideband sources without estimating the number of sources," *Signal Processing*, Vol. 92, 1032–1043, 2012.

21. Liu, C., F. Liu, and S. Zhang, "A novel direction-of-arrival estimation method for wideband signals," *Signal, Image and Video Processing*, Vol. 6, 141–145, 2012.

22. Cantrell, C., "Technical Note: Review of methods for linear least-squares fitting of data and application to atmospheric chemistry problems," *Atmospheric Chemistry and Physics*, Vol. 8, 5477–5487, 2008.

23. Yang, J., J. Thompson, X. Huang, T. Jin, and Z. Zhou, "Segmented reconstruction for compressed sensing SAR imaging," *IEEE Transaction on Geoscience and Remote Sensing*, Vol. 51, 4214–4225, 2013.

24. Wei, S.-J., X.-L. Zhang, J. Shi, and G. Xiang, "Sparse reconstruction for SAR imaging based on compressed sensing," *Progress In Electromagnetics Research*, Vol. 109, 63–81, 2010.

25. Vishal, M. P., R. E. Glenn, M. H. Dennis, and C. Rama, "Compressed synthetic aperture radar," *IEEE Journal of Selected Topic in Signal Processing*, Vol. 4, 244–254, 2010.

26. Yu, Z. and M. Liu, "Suppressing azimuth ambiguity in spaceborne SAR images based on compressed sensing," *Science China: Information Sciences*, Vol. 55, 1830–1837, 2012.